

The Gelsolin Pathogenic D187N Mutant Exhibits Altered Conformational Stability and Forms Amyloidogenic Oligomers

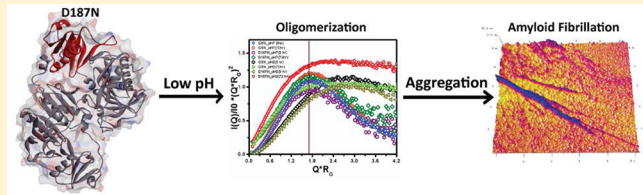
Ankit Srivastava,[†] Jasdeep Singh,[†] Shiv Pratap Singh Yadav,[‡] Prabha Arya,^{†,§} Fouzia Kalim,[†] Pooja Rose,[†] Ashish,^{*,‡} and Bishwajit Kundu^{*,†,ID}

[†]Kusuma School of Biological Sciences, IIT Delhi, New Delhi 110016, India

[‡]CSIR-Institute of Microbial Technology, Chandigarh 160036, India

Supporting Information

ABSTRACT: Gelsolin is an actin-severing protein that attains an open functional conformation in the presence of Ca^{2+} or low pH. Mutations (D187N/Y) in the second domain of gelsolin trigger the proteolytic pathway producing amyloidogenic fragments that form the pathological hallmark of gelsolin amyloidosis and lattice corneal dystrophy type 2 (LCD2). Here, we show that the D187N mutant gelsolin in a Ca^{2+} -depleted, low pH-activated, open conformation could assemble into amyloidogenic oligomers without necessarily undergoing the specific proteolytic step. Although both wild-type (WT) and mutant proteins exhibit closely overlapping globular shapes at physiological conditions, the latter exhibits subjugated actin depolymerization, loss of thermodynamic stability, and folding cooperativity. Mutant gelsolin displayed aberrant conformational unwinding and formed structural conformers with high associative properties at low pH conditions. A SAXS intensity profile and Guinier analysis of these conformers showed the formation of unusual, higher order aggregates. Extended incubation at low pH resulted in the formation of thioflavin T and Congo red positive, β -sheet rich aggregates with a fibrillar, amyloid-like morphology visible under electron and atomic force microscopy. Mass spectrometric analysis of disaggregated end-stage fibrils displayed peptide fragments encompassing the entire protein sequence, indicating the involvement of full length mutant gelsolin in fibril formation. Atomistic and REMD simulations indicated a larger increase in solvent accessibility and loss of fold architecture in mutant gelsolin at low pH as compared to WT gelsolin. Our findings support the existence of a secondary oligomerization-dependent aggregation pathway associated with gelsolin amyloidosis and can pave the way for better therapeutic strategies.



Amyloidogenesis involves the conformational conversion of native proteins or peptides into misfolded, higher order amyloid aggregates having distinct β -sheet architecture.^{1–3} These aggregates along with their prefibrillar and oligomeric species collectively contribute to cellular toxicity and tissue impairment and aid in disease manifestation.⁴ Gelsolin amyloidosis or AGel amyloidosis represents a similar case, where mutant gelsolin undergoes proteolytic cleavage producing amyloidogenic fragments that aggregate and contribute to disease etiology.⁵ Two mutant forms of gelsolin (G654A or G654T) have been found associated with familial amyloidosis and Meretoja's syndrome or lattice corneal dystrophy type 2 (LCD2).⁶ These mutations in the gelsolin gene lead to a substitution of Asp187 with either Asn (Finnish-type) or Tyr (Danish-type), respectively⁷ (Figure 1). Besides, two other mutations in gelsolin, viz., Asn184 to Lys (C633 to A) and Gly167 to Arg (G580 to A), associated with renal amyloidosis are also reported.^{8,9}

Gelsolin is a hexa-domain (named G1–G6), actin-severing, nucleating, capping protein that exists as cytosolic and secreted plasma isoforms in most vertebrates, including in humans.¹⁰ The protein exhibits a compact globular structure under Ca^{2+} -free conditions at physiological pH. It undergoes a conformational change and attains an extended, functionally active form

in the presence of 1 mM Ca^{2+} or low pH ($\text{pH} \leq 5$).¹¹ This dual activation mechanism of gelsolin is reportedly required during physiological (Ca^{2+} -regulated) as well as stressed (low pH-regulated) conditions.¹² A mutation in its second domain (G2) alters its calcium binding capacity, resulting in an aberrant conformation that makes it susceptible to proteolytic cleavage (Figure 1). Previous reports have shown that calcium binding plays an important role in imparting overall structural stability to gelsolin.^{13,14} In fact, the isolated G2 domain under calcium-free conditions folds into a non-native conformation.¹⁵ Additionally, urea denaturation studies have also shown that the D187N variant is slightly destabilized compared to wild-type (WT) gelsolin.¹⁶ However, a detailed biophysical study emphasizing the implications of the destabilized G2 domain harboring a D187N mutation under Ca^{2+} -free conditions is not yet available.

Besides, several other studies have also shown that gelsolin amyloidosis incurs high endoplasmic reticulum (ER) stress and compromises cellular functions.^{17,18} Evidently, amyloid-associated ER stress in Alzheimer's disease (AD) and kidney

Received: January 12, 2018

Revised: March 15, 2018

Published: March 30, 2018



ACS Publications

© XXXX American Chemical Society

A

DOI: 10.1021/acs.biochem.8b00039
Biochemistry XXXX, XXX, XXX–XXX

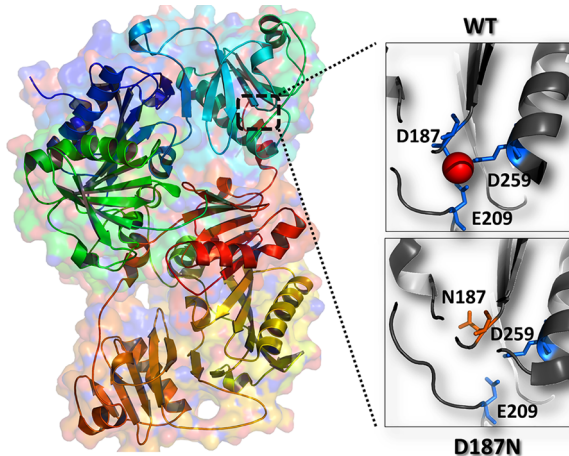


Figure 1. Gelsolin multidomain architecture. Structure of gelsolin monomer (PDB entry 3FFN) depicting all six domains (G1–G6) in different colors. The zoomed view of the second (G2) domain (turquoise) shows the position of aspartic acid (D187) in WT protein and the point mutation incorporating an asparagine residue (N187) in the mutated (D187N) protein. A loss in Ca^{2+} binding (red sphere) due to D187N mutation is also shown. The structures were visualized using UCSF Chimera.

amyloidosis also induce lactic acidosis, hypokalemic acidosis, and tubular acidosis that could facilitate the release of metal ions from metal binding proteins like gelsolin.^{19–22} In the context of gelsolin amyloidosis, cellular acidosis could create an intriguing combination of misfolded, yet partially active, conformations of gelsolin protein. Interestingly, a recent report by Bannykh and co-workers showed the presence of distinct amyloid fibers inside the ER of mice expressing a mutant (D187N) form of gelsolin.²³ A similar alteration in the processing of β -amyloid precursor protein (APP) with an increase in brain lactate production in AD has also been reported.²⁴ This led us to hypothesize that during progressive phases of gelsolin amyloidosis, loss in calcium regulation could drive acidosis-like conditions, thereby propelling mutant gelsolin to attain an open and partially active conformation. To reliably understand the biophysical implications of this scenario, we studied the open conformation of WT and D187N mutant gelsolin under low pH conditions using a battery of spectral and ultrastructural probes. Our results provide insights into how the D187N mutation reduces structural integrity in gelsolin, thereby populating an amyloidogenic precursor state that oligomerizes into amyloid-like aggregates under low pH conditions.

MATERIALS AND METHODS

Preparation of Proteins. A pRSET-A plasmid incorporating the human plasma gelsolin gene cloned between the *Bam*H I and *Hind*III restriction sites was used. The protein was expressed and purified using anion exchange followed by gel filtration chromatography as described elsewhere.¹² The purified protein incorporates an N-terminal His-tag and a few pRSET-A vector-associated extra amino acids. Since the extra amino acids have no discernible effect on the structure/activity and actin-depolymerization property of gelsolin, all of the experiments were performed using His-tagged protein. The mutant gelsolin (G654A) was created by site-directed mutagenesis employing a protocol from the Quikchange site-directed mutagenesis kit from Stratagene (Agilent Technologies,

USA). A single point mutation in gelsolin (WT) at position 187 (D187N) by replacing the aspartic acid residue with an asparagine using partially overlapping primers was done. The following primers were utilized with the newly introduced base underlined: 5'-G GAG AGC TTC AAC AAT GGC AAC TGC TTC ATC CTG GAC CTG-3' and 5'-CAG GTC CAG GAT GAA GCA GTT GCC ATT GTT GAA GCT CTC C-3'. The mutation was verified by sequencing at Chromous Biotech, India. After mutation confirmation and a protein expression check, the D187N variant was purified using a similar protocol as described above. The concentrations of GFC purified proteins was measured using UV absorption at $A_{280} \sim 1.4$, corresponding to 1 mg mL⁻¹ (DU-640 spectrophotometer, Beckman). To confirm the molecular weight and monodispersity of both gelsolin variants, 100 μL of each protein sample (1 mg mL⁻¹) was loaded onto a precalibrated superdex 200, 10/300 SEC column attached to an AKTA purifier system (GE Healthcare, USA) operated at 25 °C. Further, molecular masses of the proteins were also confirmed by mass spectrometry.

Fluorescence and Circular Dichroism (CD). Tryptophan fluorescence spectra were measured using a 10 mm path length quartz cuvette in an LS 55 spectrofluorimeter (PerkinElmer, MA, USA) at 25 °C. The excitation wavelength was fixed at 295 nm, and the spectra were recorded between 310 and 400 nm. For all experiments, protein concentrations were kept constant at 3.6 μM . For far-UV CD measurements, all protein samples were scanned (250–200 nm) in a 1 mm path length cell at 25 °C using a J810 spectropolarimeter (JASCO). The mean residual ellipticity $[\theta]$ in each case was calculated using eq 1:

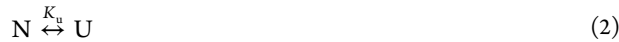
$$[\theta] = \frac{\theta_{\text{obs}} \times \text{MRW}}{10lc} \quad (1)$$

Here, θ_{obs} is the observed ellipticity in millidegrees (mdeg), and MRW (mean residue weight) represents $M/(N - 1)$ (M is molecular weight and N is number of residues). The variable c is the concentration in mg mL⁻¹, and l is the path length in cm.

Thermal Denaturation Assay. For thermal denaturation experiments, change in ellipticity $[\theta_{210}]$ was monitored against temperature with a ramping rate of 1 °C/min. All data were recorded in triplicate, and the averaged spectra was normalized, fitted using the Origin 8.0 software, and reported.

Equilibrium Unfolding/Refolding Experiments. All equilibrium unfolding/refolding experiments were carried out using 8 and 10 M stocks of ultrapure GdnCl and urea, respectively. For unfolding studies, protein samples were prepared in Tris buffer (25 mM Tris, 50 mM NaCl, pH 7) containing varying concentrations of denaturant (GdnCl or urea), followed by equilibration for 12 h at 25 °C. Similarly, for refolding studies, protein stocks (50 μM) unfolded in 6 M GdnCl/urea for 24 h were stepwise diluted in Tris buffer and further left for a 12 h equilibration at 25 °C. A final protein concentration of 2.5 μM was kept constant for all unfolding/refolding experiments. Fluorescence scans of each sample taken in a 1 cm cuvette were recorded between 310 and 400 nm, after excitation at 295 nm, in an LS 55 spectrofluorimeter (PerkinElmer, USA). The excitation and emission slits were fixed at 5 nm each. The ratio of fluorescence emission at 360 and 332 nm (334 nm for D187N) was calculated and plotted against increasing concentration of GdnCl or urea. Finally, the data were analyzed assuming the free energy of unfolding or refolding (G_D^0) to be linearly dependent on the denaturant concentration. G_D^0 was obtained by linear extrapolation of the

plot of free energy change and denaturant concentration to 0 M. The pattern of unfolding and refolding of each gelsolin variant was analyzed and approximated in a two-state unfolding model described by the following reaction (eq 2):



Here, N and U are the molar concentrations of native and unfolded proteins, respectively, and K_u is the unfolding rate constant. The data of denaturant-induced transition curves were analyzed using a nonlinear least-squares method for obtaining free energy change of unfolding in the absence of any denaturant (G_D^0), the midpoint concentration of denaturant required for unfolding or refolding (C_m), and the slope (m) of the unfolding or refolding curve at C_m using the following eqs 3–6, as described previously:²⁵

$$K_u = [(y)_N - (y)]/[(y) - (y)_U] \quad (3)$$

$$\Delta G_D = G_D^0 - m[D] \quad (4)$$

$$K_u = e^{(m[D] - \Delta G_D^0/RT)} \quad (5)$$

$$C_m = -(\Delta G_{(H_2O)}/m) \quad (6)$$

Here, $(y)_N$ and $(y)_U$ are optical properties of the native and denatured protein molecules, respectively. R is the universal gas constant, and T is the temperature in kelvin; ΔG_D is the change in free energy at a particular denaturant concentration [D].

Amyloid Aggregation Experiments. Both purified proteins (WT and D187N gelsolin) were incubated at a concentration of 2–10 μ M in different pH buffer solutions (pH 2–10) with a 0.02% (v/v) final concentration of sodium azide. All samples (250 μ L) were incubated in 1.5 mL eppendorfs at 37 °C under continuous agitation at 200 rpm and monitored by dye binding assays.

Dye Binding Assays. For the ThT assay, samples (10 μ L) aliquoted at different time points were mixed with 10 μ M ThT (90 μ L) prepared in 50 mM phosphate buffer (pH 7) and incubated for 10 min. Following this, fluorescence readings ($\lambda_{\text{excitation}} = 450$ nm, $\lambda_{\text{emission}} = 485$ nm) were recorded in a 1 cm path length cuvette using an LS 55 fluorescence spectrometer (PerkinElmer, MA, USA), while the excitation and emission slits were kept at 5 and 10 nm, respectively. Data from triplicate reactions were averaged and fitted using sigmoid eq 7 in Origin 8.0, as described earlier.²⁶

$$Y = (Y_i + m_i x) + \frac{Y_f + m_f x}{1 + \exp \frac{-(x - t_{50})}{\tau}} \quad (7)$$

Here, Y is the ThT fluorescence intensity (a.u.). τ is the time constant. x is the time in hours, and t_{50} is the time at which ThT fluorescence attained 50% of the maximum intensity (I_{max}). The lag time of aggregation (T_{lag}) was calculated using eq 8.

$$T_{\text{lag}} = t_{50} - 2\tau \quad (8)$$

For the Congo red (CR) binding assay, the aggregates were incubated with 600 μ L of CR solution (9.2 mM in PBS) at room temperature for 4 h in the dark. The absorption spectra between 400 and 600 nm were recorded using a DU-640 spectrophotometer (Beckman), with subtraction of the baseline spectrum of the buffer. The absorbance spectrum of each sample was also corrected for light scattering by subtracting the spectra of aggregates alone in the buffer scanned in the visible

region. The final spectrum obtained for each sample was compared with CR-only spectra to ascertain the characteristic amyloid-bound red-shift.

For the surface hydrophobicity assessment, 1-anilinonaphthalene 8-sulfonate (ANS) binding experiments were performed. After we added the ANS dye to different protein samples at a final concentration of 50 μ M, the samples were incubated for 5 min at 25 °C. Following this, fluorescence scans in the range of 400–600 nm ($\lambda_{\text{excitation}} = 370$ nm) were recorded in a 1 cm path length cuvette using an LS 55 fluorescence spectrometer (PerkinElmer, MA, USA), while the excitation and emission slits were kept at 5 nm each.

Transmission Electron Microscopy (TEM). Transmission electron micrographs of aggregating samples were recorded using a Tecnai transmission electron microscope (FEI, USA) operated at 120 kV. The aggregates obtained after a 1 week incubation were 5-fold diluted and placed on a copper grid for 2 min. Following this, samples were negatively stained using a 2% (w/v) uranyl acetate solution, washed with Milli-Q water, air-dried, and imaged.

Atomic Force Microscopy (AFM). AFM imaging of aggregate samples was done using a Bioscope Catalyst AFM (Bruker Corporation, Billerica, MA). The end-stage morphology of gelsolin aggregates formed after a 1 week incubation was examined. Each sample was diluted 3-fold in 50 mM phosphate buffer (pH 7.0) and deposited on freshly cleaved mica. Following a 30 min incubation, the samples were washed using Milli-Q water and dried overnight. Samples were analyzed using standard tapping mode, and the resulting images were processed using Nanoscope analysis version 1.4.

SAXS Data Acquisition. SAXS data were collected on a synchrotron BM-29 beamline at the European synchrotron radiation facility (ESRF), Grenoble, France. In each case, 30 μ L of sample and buffer were exposed to X-rays while flowing through the 1.8 mm-diameter quartz capillary using the sample-changer robot for 10 s at 10 °C. Scattered X-rays were detected by using a 1 M pilatus detector with a detector distance of 2.867 m. Initial data analysis was done using beamline software, BsxCuBE²⁷ (Biosaxs Customized Beamline Environment). The desmeared and subtracted files obtained by BsxCuBE software were further processed using ATSAS suite 2.8.2.

SAXS Data Analysis and Modeling. The desmeared $I(Q)$ files were analyzed using Guinier analyses presuming a globular and rod-like scattering shape of the scattering particles which yielded the radius of gyration (R_g) and the radius of cross section (R_c). These analyses were done using the SAS data analysis program in the ATSAS 2.8.2 suite of programs. Kratky plots ($I(Q) \times Q^2$ vs Q) of each data set were prepared to examine the nature of scattering protein in the solution. After confirmation of the globular scattering profiles, the distance distribution program of SAS data analysis was employed to perform indirect Fourier transformation of the scattering data to obtain a pairwise distribution function of interatomic vectors, $P(r)$. During the transformation, the probability of finding a pairwise vector equal to 0 Å and the maximum linear dimension (D_{max}) was considered to be zero. To visualize the predominant solution shape of each protein, 10 independent uniform density models were generated using Dammin software for each data set. Finally, the refined and averaged models were used for comparison and superimposition with the crystal structure (PDB entry 3FFN).

Mass Spectrometry. An Ultraflex Extreme MALDI-TOF/TOF mass spectrometer (Bruker Daltonics, Germany) was

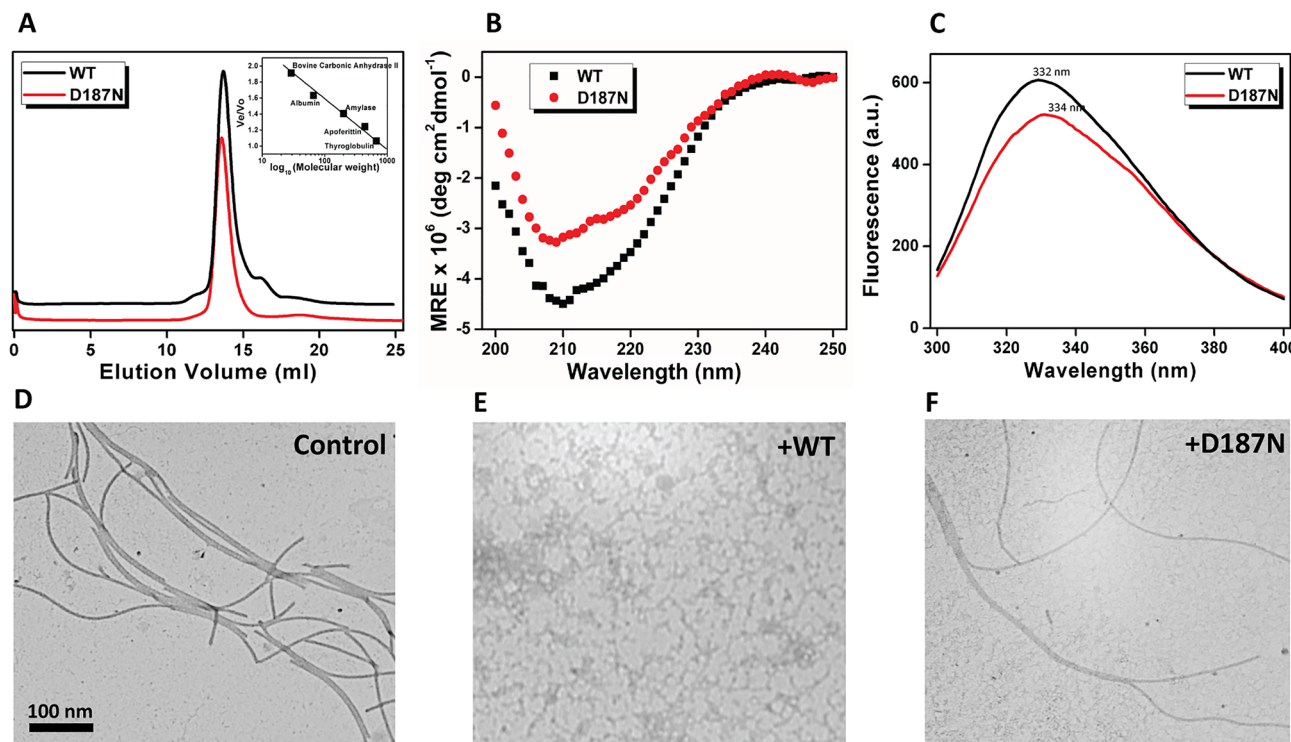


Figure 2. Comparative biochemical profiles of WT and D187N mutant gelsolin. (A) Size-exclusion chromatography profile of WT (black) and mutant gelsolin (red). The inset shows the standard curve for a Superdex 200 10/300 GL column. (B) Far-UV CD spectra. (C) Intrinsic tryptophan fluorescence emission curves. (D–F) Visualization of F-actin-depolymerization activities of both gelsolin variants. F-actin was incubated with buffer alone (control, 50 mM Tris buffer, pH 7.5) or with either gelsolin variant at a molar ratio of 1:5 (gelsolin/actin) in buffer containing 1 mM CaCl_2 , and the depolymerization activity was observed by negative stain electron microscopy after a 2 h incubation. Scale bars represent 100 nm in each case.

used for determining intact protein mass and identification of peptides incorporated in the amyloid aggregates. End-stage amyloid aggregates were aliquoted in microcentrifuge tubes that were rinsed in USP-grade ethanol followed by Milli-Q water and air-dried before use. In order to disaggregate the fibrils, urea was added to a final concentration of 6 M (100 μL in Tris buffer), and the samples were incubated overnight at room temperature. Following this, DTT was added to a final concentration of 10 mM, and samples were left for an additional 1 h incubation time. Next, sample alkylation was achieved by adding iodoacetamide to a final concentration of 40 mM, and the samples were incubated for 1 h at room temperature. After this, Milli-Q water was added to the samples to decrease the final urea concentration to \sim 0.6 M for optimal trypsin activity. Trypsin was added (\sim 20 μg) to the samples, and digestion was carried out overnight at 37 °C. The next day, the reaction was stopped, and the samples were concentrated by evaporation, mixed with trifluoroacetic acid (0.1% v/v), and taken up in a C18 ZipTip (Pierce, Thermo Fisher Scientific, USA). Finally, the samples were stepwise eluted with increasing concentrations of acetonitrile (20–60% v/v) in trifluoroacetic acid (0.1% v/v). Samples were analyzed using MALDI-TOF/TOF MS in linear mode with sinapinic acid as the matrix. The generated peptides were analyzed and catalogued using Compass HyStar 3.2, Data Analysis 4.1, and BioTools 3.2 software (Bruker Daltonics). Further identification was done using MS/MS ion search through the Mascot search engine with a mass tolerance of \pm 0.5 Da and a maximum missed cleavage of 1.

Replica Exchange Molecular Dynamics (REMD) Simulations. The available X-ray crystal structure of WT gelsolin (PDB entry 3FFN) was utilized for all MD simulations. The systems are described in the *Supplementary Methods of the Supporting Information*. REMD enhances the conformational sampling by allowing the exchange of configurations between multiple replicas simulated over a wide range of temperatures in parallel.²⁸ The exchange of configurations allows crossing of energy barriers as they travel from lower temperature replicas to higher temperature replicas with the canonical Boltzmann distribution preserved in all replicas. In our study, we have used 50 replicas in the temperature range of 310–370 K with an optimal distribution of temperatures to achieve exchange probability of \sim 0.2–0.3. Exchanges have been attempted every 1 ps. Initially, *NVT* equilibration runs were performed using a V-rescale thermostat for \sim 2 ns at each temperature. The *NVT* production run was continued for 100 ns for each replica, amounting to a cumulative run length of 5 μs . In all simulations, the particle mesh Ewald method was used to describe the long range electrostatic interactions with a Leap frog integrator with an integration time step of 2 fs being used to solve Newton's equation of motion, and trajectories have been saved every 50 ps.

RESULTS

Preparation of Recombinant Wild-Type and Mutant Gelsolin. Both the WT and D187N mutant proteins were bacterially overexpressed and purified using anion exchange and size-exclusion chromatography as described in *Materials and Methods*. The molecular masses of the purified recombinant

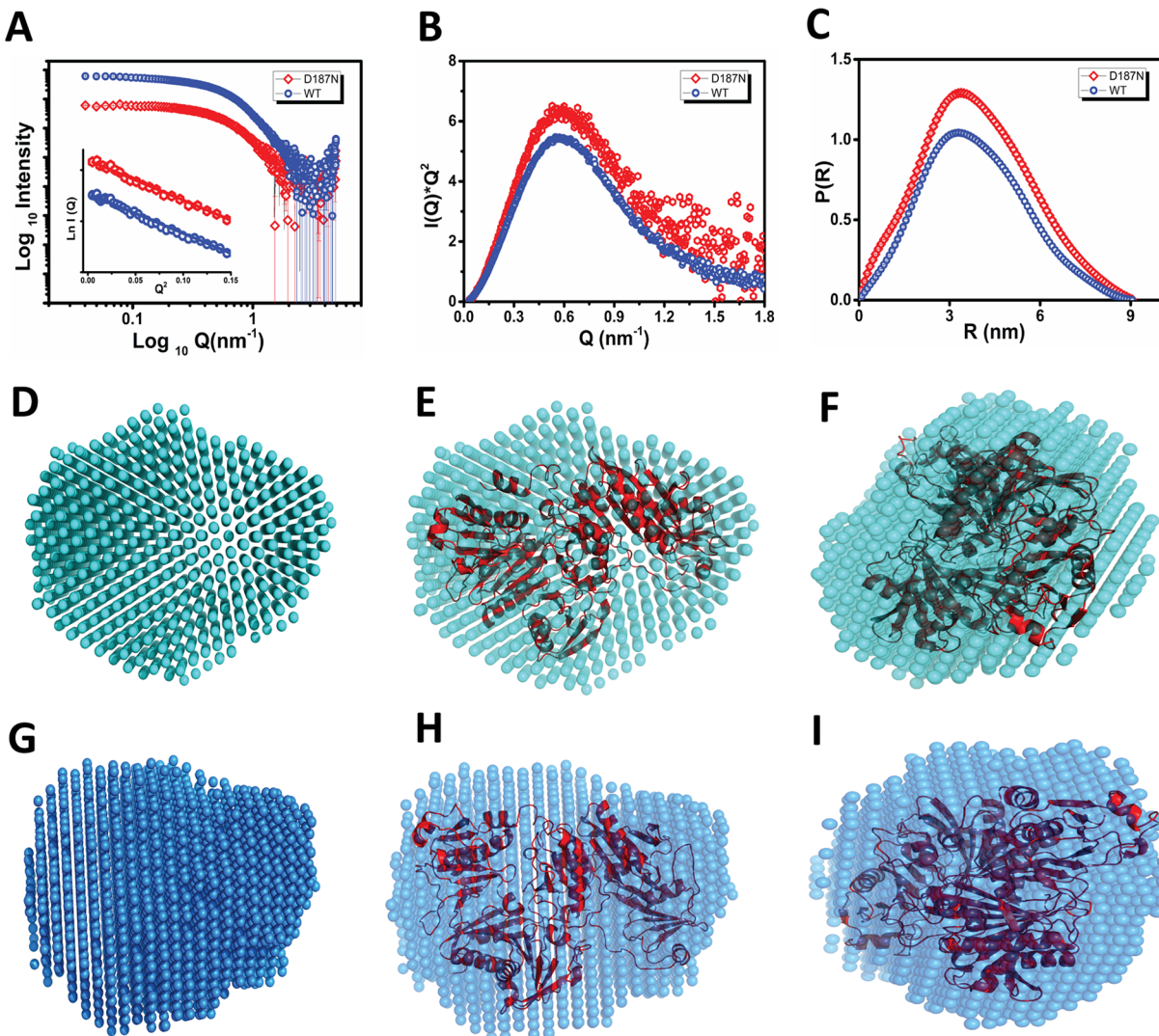


Figure 3. Structural comparison of WT and D187N gelsolin variants. (A) SAXS data profile showing double logarithmic intensity versus Q plot for WT (blue) and D187N (red) gelsolin. The inset shows a linear fit in the Guinier region. (B) Kratky plot for the WT and mutant gelsolin. (C) Pairwise distribution plot for WT and mutant gelsolin. SAXS envelopes of WT gelsolin (D–F) and D187N mutant gelsolin (G–I) and their overlay with the crystal structure of gelsolin (PDB entry 3FFN) shown in different orientations.

proteins were determined by SDS-PAGE and MALDI-MS as ~ 88 kDa (Figures S1 and S2). Further, when checked for monodispersity using analytical size-exclusion chromatography (SEC), the WT and mutant gelsolin showed uniform peaks with retention volumes of 13.7 and 13.5 mL, respectively (Figure 2A). This suggested a monomeric nature for both of the proteins under physiological conditions. A slight decrease in the retention volume of the mutant protein was observed, which could be due to partial opening of the G2 domain as reported earlier.^{29,30} All data were determined for Ca^{2+} -free proteins (in the presence of 1 mM EGTA), and further experiments were carried out under similar conditions unless mentioned explicitly.

The D187N Mutation Alters Fold Architecture and Actin-Severing Activity. The secondary and tertiary structures of both proteins were analyzed using far-UV CD and intrinsic tryptophan fluorescence, respectively. The far-UV CD spectra of the WT gelsolin showed a negative peak at 210 nm with a depression at 215 nm, indicating a mixed α/β -type secondary structure which was in accordance with the available crystal data³¹ (Figure 2B).

The mutant, however, showed a marginal shift in both of these peaks indicating an alteration in its secondary structure as compared to that of the WT protein. Upon analysis of secondary structural content at physiological conditions (pH 7), a significantly reduced α -helicity ($>45\%$) was noted for the mutant protein (Table S1). Further, the tryptophan emission profile showed maxima at 332 and 334 nm for WT and mutant proteins, respectively (Figure 2C). A red-shift in the mutant protein suggested an increase in solvent exposure of tryptophan residues. Since the G2 domain containing the D187N mutation is partially opened, we speculate the increase in solvent exposure to tryptophan residues (W180, W200; Figure S4) inside this domain. However, the contribution of other tryptophan residues close to the G2 domain also cannot be ruled out. Further, we found that the D187N mutant gelsolin exhibited a considerable loss in its ability to sever filamentous actin as compared to the WT protein (see Supplementary Methods). Electron microscopy showed that WT gelsolin reduced actin filaments of $\sim 10\text{--}12$ nm dimensions to smaller fragments and monomers ($\sim 2\text{--}4$ nm) efficiently. In contrast, after similar incubation periods, the D187N mutant gelsolin

Table 1. Structural Parameters of SAXS Data Collected for Wild-Type (WT) and D187N Mutant Gelsolin and Their Variations after 0 and 72 h of Incubation As Deduced from Guinier Analyses and Indirect Fourier Transformation

protein	0 h					72 h				
	Guinier analyses			Indirect Fourier Transformation		Guinier analyses			Indirect Fourier Transformation	
	R_g (nm)	R_c (nm)	L (nm)	D_{max}	R_g (nm)	R_g (nm)	R_c (nm)	L (nm)	D_{max}	R_g (nm)
WT (pH 7)	3.27	1.65	11.2	9.1	3.02	3.29	1.7	9.76	9.2	3.24
D187N (pH 7)	3.28	1.69	11.23	9.13	3.07	3.59	1.73	10.9	9.3	3.12
WT (pH 2)	5.23	2.16	16.5	17	5.51	5.28	2.1	16.7	18	5.51
D187N (pH 2)	6.06	2.32	20.8	22	6.9	a	a	a	a	a

^aCould not be computed.

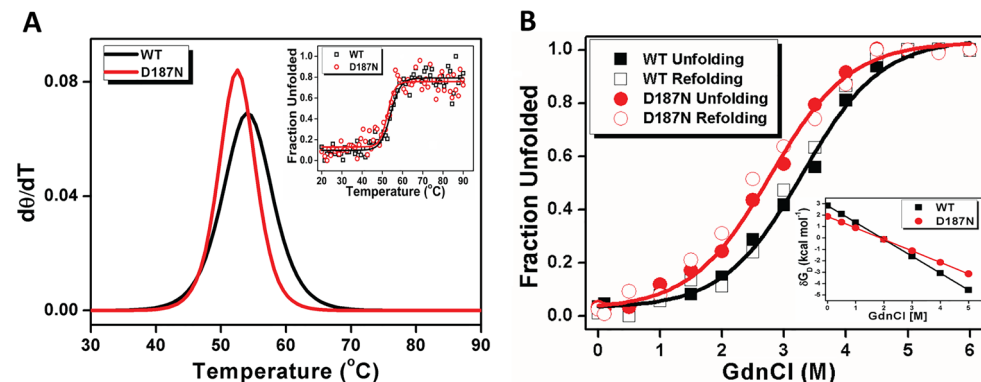


Figure 4. Comparative assessment of thermodynamic stability. (A) Thermal denaturation of WT (black) and D187N mutant gelsolin (red) probed by monitoring secondary structure changes (θ_{210}) with increasing temperature. First derivatives ($d\theta/dT$) of normalized melting curves are shown where the maxima indicate T_m (melting temperature) of the corresponding system. The inset shows normalized raw data represented as percent unfolding induced by temperature increments for both systems. (B) Normalized equilibrium unfolding and refolding curves of gelsolin variants at pH 7.0 after 12 h of incubation at 25 °C. In each case, the plot of the fractional change in the wavelength maxima of the intrinsic tryptophan fluorescence of the WT (black) and mutant (red) gelsolin with increasing molar concentrations of GdnCl is shown. The inset shows the linear free energy extrapolation curve of WT and D187N mutant proteins with respect to GdnCl concentrations. The free energy in the absence of denaturant (G_D^0) is the intercept on the y -axis, obtained using the linear extrapolation method.

incubated samples still showed a significant population of intact actin filaments (Figure 2D–F).

WT and Mutant Gelsolin Exhibit Similar Global Shapes at Physiological Conditions. To gain insights into the global shape and quaternary structure, SAXS data profiles from solutions of both of the proteins were analyzed. Data acquired from solutions of WT and D187N mutant gelsolin in a physiological buffer (50 mM TrisCl, pH 7) under calcium-free conditions and a 24 h incubation were analyzed, and the shapes were constructed. SAXS Intensity $I(Q)$ profiles indicated a lack of aggregation or interparticulate nature in both WT and mutant gelsolin samples (Figure 3A). Monodispersity in the samples was confirmed by a linear fit in the Guinier region (inset, Figure 3A). The slope of the linear fit in the Guinier region yielded R_g values of 3.27 and 3.28 nm for the WT and mutant gelsolin, respectively, presuming the globular nature of the scattering particle in both samples (Table 1). Similarly, R_c values were found to be 1.65 and 1.69 nm, respectively, presuming a rod-like nature of the scattering particle. From these R_g and R_c values, the theoretical persistent length (L) of the scattering particle was calculated as ~11.2 nm for both proteins. Further, Kratky analysis also confirmed the globular nature of both proteins (Figure 3B). $P(r)$ analysis done by the distance distribution function of SAXS data using the indirect Fourier transformation showed similar D_{max} values for WT and mutant gelsolin, at ~9.1 nm (Figure 3C). Additionally, volume correlation (V_C)-based analysis of scattering particles using the DATMOW program yielded molecular mass values (87.6 and

88.2 kDa, respectively) very close to that of monomeric proteins and in agreement with the SEC profile. Subsequently, global shapes of the proteins in solution were computed using SAXS data profiles. The generated SAXS envelopes were then superimposed on the available crystal structure of gelsolin³¹ (PDB entry 3FFN). Shape restoration after automated alignment of inertial axes of SAXS-based envelopes using SUPCOMB largely matched the crystal structure and affirmed the compact globular shape of both proteins (WT, Figure 3D–F; D187N, Figure 3G–I).

The D187N Mutation Decreases the Thermodynamic Stability of Gelsolin. The relative structural stabilities of the two proteins were studied by thermal unfolding at pH 7. Far-UV CD spectra (210 nm) were monitored as a function of increasing temperature. Both WT and mutant gelsolin unfolded with a single transition over the temperature range of 20–90 °C (Figure 4A). Both of the proteins started to lose native secondary structure (change in 210 nm band) above 45 °C and precipitated into large visible aggregates beyond 60 °C with an apparent loss of CD signal. Since the thermal refolding curves were irreversible, a reliable estimate of free energy (ΔG) could not be determined. The resulting curves were analyzed, and T_m (melting temperature) was calculated. T_m is the temperature where half of any protein population is denatured and thus can be used for a comparative estimate of stability between two proteins. The T_m values of WT and mutant gelsolin were found to be ~54 and 51 °C, respectively, indicating a destabilizing effect of the D187N point mutation (Table 2).

Table 2. Conformational Stability Parameters of the WT and D187N Mutant Gelsolin Proteins^a

protein	Thermal denaturation		GdnCl unfolding/refolding	
	T_m (°C)	ΔG_D^0 (kcal mol ⁻¹)	M (kcal mol ⁻¹ M ⁻¹)	C_m (M)
WT	54.1 ± 0.4	2.8 ± 0.1	1.5 ± 0.1	1.9 ± 0.2
D187N	51.5 ± 0.5	1.9 ± 0.2	1.1 ± 0.1	1.7 ± 0.1

^aThe melting temperatures (T_m) for WT and D187N gelsolin were calculated from CD thermal denaturation curves (θ_{210}). Unfolding studies were done at various concentrations of urea and GdnCl as described in Materials and Methods. The C_m and ΔG_D^0 values are based on three independent experiments for each measurement and are represented as mean and standard deviation. All experiments were carried out at pH 7.

Further, the destabilizing effect of the D187N mutation was studied using equilibrium unfolding experiments. The intrinsic tryptophan fluorescence for both proteins was monitored against increasing denaturant (urea and GdnCl) concentrations. Interestingly, even in the presence of >5 M urea, both proteins

resisted complete unfolding as the λ_{max} did not shift beyond 347 nm, indicating only partial unfolding.

However, in the presence of GdnCl, both proteins started to show gradual unfolding starting at 1 M GdnCl ($\lambda_{max} = 341$ nm, WT; $\lambda_{max} = 345$ nm, D187N), reaching complete unfolding at 2.5–3.0 M GdnCl ($\lambda_{max} = 352$ nm, WT; $\lambda_{max} = 356$ nm, D187N) (Figure S5). The unfolding curves overlapped with the refolding curves for both proteins, indicating attainment of equilibrium. Both proteins exhibited a sharp sigmoidal transition, suggesting cooperative unfolding/refolding through a reversible two-state process (Figure 4B). The data were fitted according to the nonlinear equation described in Materials and Methods, and values of free energy in the absence of denaturant (G_D^0), cooperativity (m), and the midpoint of unfolding transition (C_m) were obtained for each system (Table 2). As per the fits, G_D^0 and m values calculated for WT were 2.8 kcal/mol and 1.5 M, respectively, and for the D187N mutant were 1.9 kcal/mol and 1.1 M, respectively. Lower G_D^0 and m values observed for mutant gelsolin indicated a loss of stability and cooperativity due to destabilization of the protein structure. Also, a comparatively lower denaturant concentration was

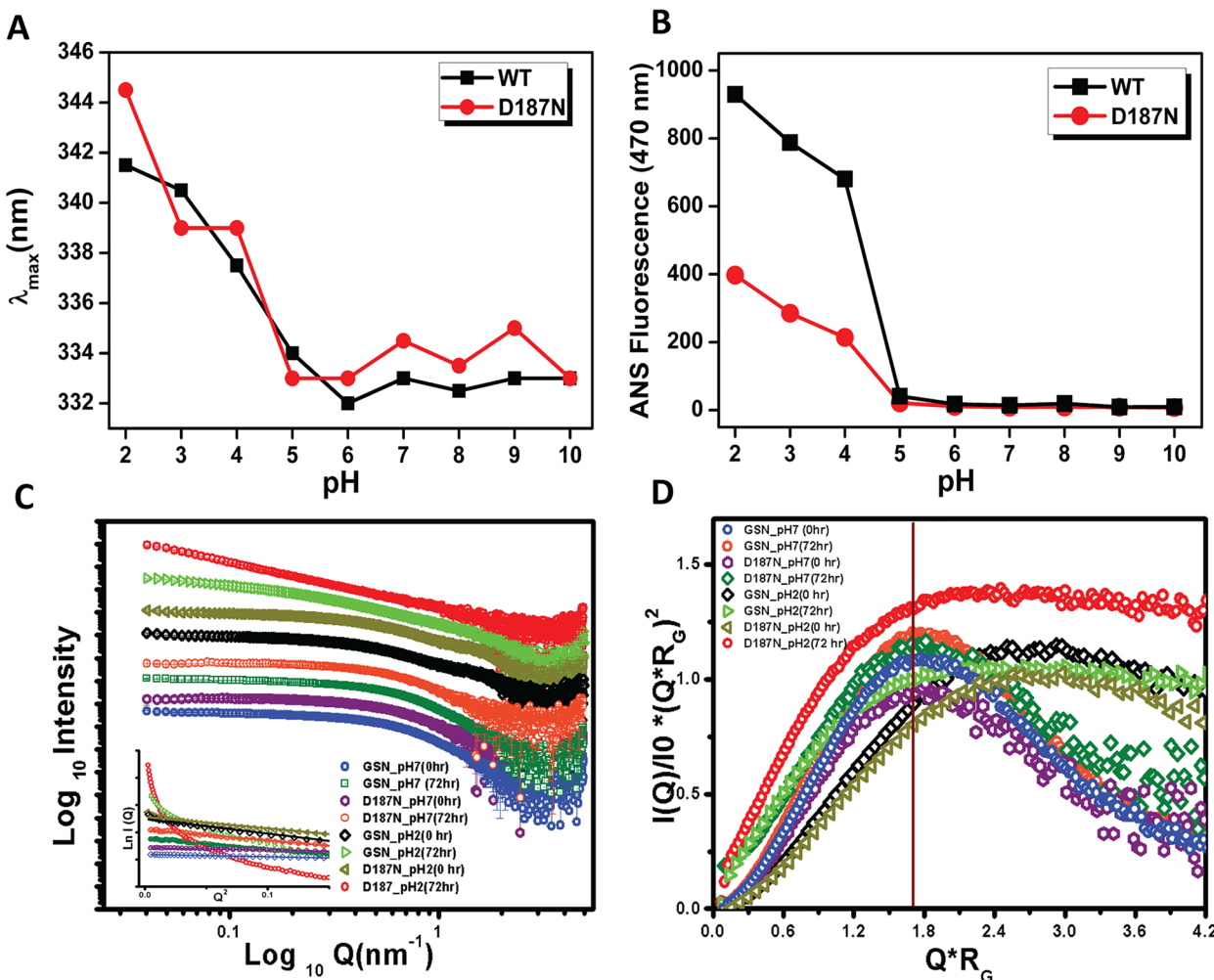


Figure 5. Assessment of pH-based structural transitions in gelsolin variants. (A) Tertiary structural changes monitored by changes in intrinsic tryptophan fluorescence (λ_{max}) with pH gradient. **(B)** Surface hydrophobicity changes monitored by ANS fluorescence (intensity_{max}) with pH gradient. **(C)** SAXS data based on a double logarithmic plot of intensity versus Q for gelsolin variants incubated at pH 7 and 2 for 0 and 72 h. The inset shows fits in the Guinier region for all systems. **(D)** Kratky plot for gelsolin variants incubated at pH 7 and 2 for 0 and 72 h. A vertical line demarcates the peaks close to 1.73 depicting the globular shape. All systems are indicated with mentioned color traces.

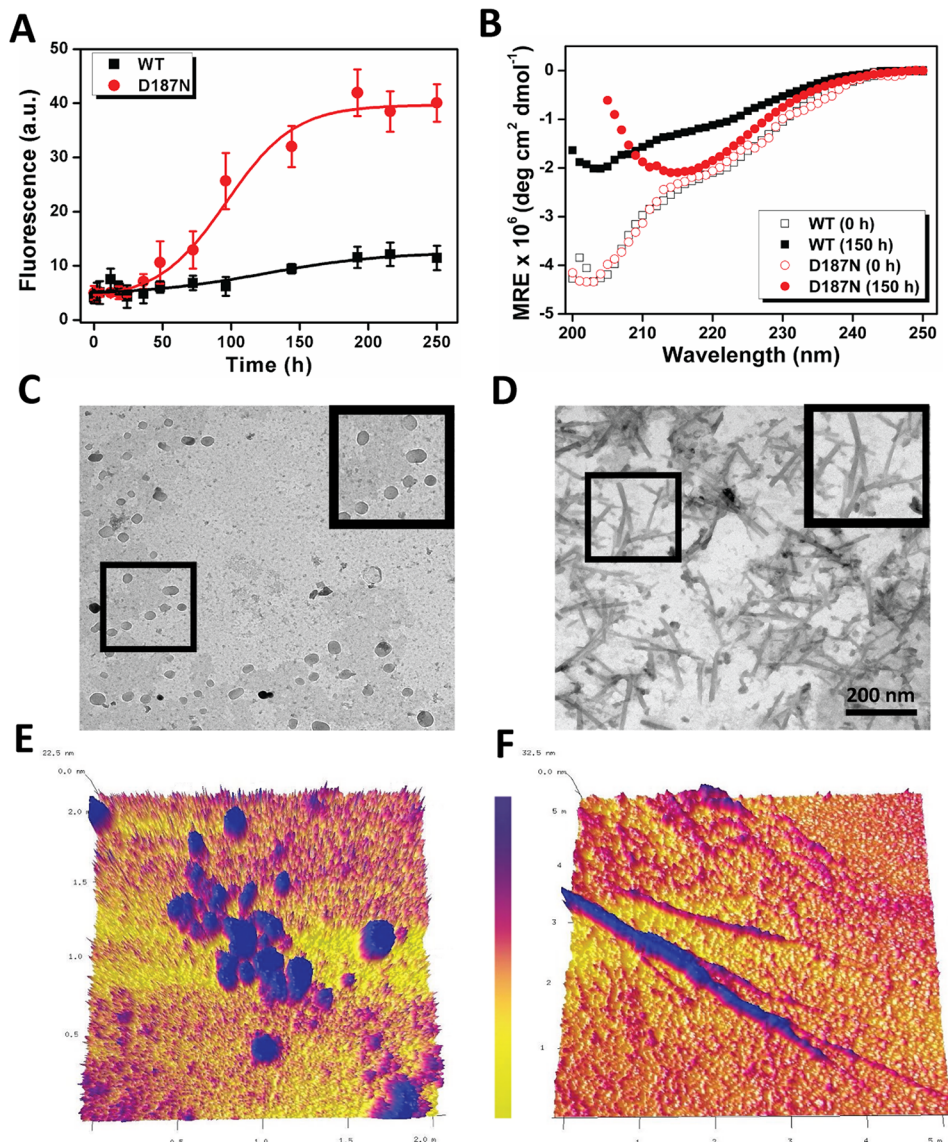


Figure 6. Characterization of aggregation in gelsolin variants. (A) Changes in ThT fluorescence plotted as a function of time to represent aggregation kinetics of WT (black) and D187N mutant gelsolin (red) proteins. (B) Circular dichroism-based secondary structural assessment of native proteins (WT and D187N) and their aggregates formed after a 150 h incubation under pH 2 conditions. Assessment of aggregate morphology by negative stain electron microscopy and atomic force microscopy for aggregates formed by WT (C–E) and mutant gelsolin (D–F). The images were taken after a 1 week incubation in each case.

required to unfold the mutant protein as evident from a decrease in the C_m value.

The D187N Mutant Exhibits Altered Conformation and a Higher Rate of Aggregation at Low pH. At this stage, we were interested in understanding the implications of the destabilized nature of mutant gelsolin under Ca^{2+} depleted, low pH conditions. This is important since gelsolin, which otherwise attains an actin-competent, open structure in the presence of Ca^{2+} , also unwinds into a similar conformation at low pH.¹² Upon equilibration with different buffers in a range of pH values, a gradual opening of the structure was observed in both of the gelsolin variants at acidic pH. From the far-UV CD signatures of both of the proteins, we found that they gradually lose their native α/β conformation during stepwise lowering of pH (Figure S3). As discussed earlier, the mutant gelsolin harbored natively lower helical content at pH 7 that decreases drastically on further lowering of the pH. Interestingly, the loss of helicity in the WT protein (~70%, pH 7 to 2) was

comparatively higher than that in the mutant protein that also showed relatively higher residual β -sheet content at pH 2 (Table S1). Further, tertiary structural changes studied using fluorescence spectroscopy showed a cooperative increase in λ_{max} (332 to 342 nm) of WT gelsolin in the acidic pH range (pH 6 to 2), indicating exposure of buried tryptophans (Figure 5A). Interestingly, the D187N mutant remained in a closed conformation until pH 5 ($\lambda_{\text{max}} = 334$ nm) and showed an abrupt increment in λ_{max} (339 nm, pH 4) at lower pH values. At low pH, striking differences were observed between the mutant and the WT proteins. The mutant gelsolin exhibited a tertiary structural perturbation at pH 2 ($\lambda_{\text{max}} = 345$ nm) larger than that of the WT gelsolin ($\lambda_{\text{max}} = 341$ nm).

To further validate the tertiary structure perturbation and exposure of tryptophans in both proteins, we performed tryptophan (Trp) quenching experiments using acrylamide (Figure S6). The acrylamide quenching experiments divulged information about changes in the local environment of

tryptophan residues in proteins. A higher Stern–Volmer quenching constant (K_{sv}) indicates higher accessibility of Trps to the quencher acrylamide. Interestingly, at pH 2, the D187N mutant exhibited a significantly lower K_{sv} value (>50% reduction) as compared to the value for WT gelsolin, indicating lower penetration of the quencher (Table S2). This indicated a subdued hydrophobic exposure in the mutant protein even at a very low pH. Our notion was corroborated by the considerable difference in hydrophobicities between the WT and mutant proteins under identical conditions. ANS fluorescence (depicting surface hydrophobicity) of the mutant gelsolin remained at least 4-fold lower than that of the WT protein at low pH values (pH 5 to 2, Figure 5B). With no visible precipitation and in the absence of complete unfolding (as achieved by GdnCl > 3 M, $\lambda_{max} = 355$ nm, Figure S5), this decreased surface hydrophobicity of the mutant gelsolin could be due to sequestration of hydrophobic patches during the formation of soluble oligomers.

To ascertain this, we next investigated the particle size profile of gelsolin variants equilibrated at different pHs using DLS (Figure S7). We found that mutant gelsolin exhibited a dramatic increase in size distribution extending from hydrodynamic radii (R_h) of 5–7 nm at pH 7 to 100–140 nm at pH 2. Under identical conditions, the R_h values for the WT protein, however, showed only a gradual rise with particle sizes ranging between 15 and 18 nm. Together, these results indicate that mutation-induced destabilized structural conformers of gelsolin promote extensive protein–protein interactions to form higher order oligomeric structures.

To get the structural perspective, we analyzed the SAXS data profiles and found that both proteins showed significantly high intensities when incubated at pH 2 as compared to pH 7 (Figure 5C). The observed high intensity depicts a polydispersed oligomeric nature of proteins in solution. The intensity plots at pH 2 showed an upward trend at a low Q range hinting toward rod-shaped protein aggregates. Interestingly, the intensity at pH 2 was found to be significantly higher for the mutant gelsolin as compared to that of the WT gelsolin. This directly correlates to a higher extent of structural unwinding and interprotein associations (high R_g) in the mutant gelsolin, enforcing higher aggregation as compared to that of the WT. Further, extended incubation at pH 7 (up to 72 h) showed only minor changes in SAXS shape parameters for both proteins with the least deviation in R_g and R_c values, indicating marginal structural perturbation (Figure 5C, Table 1).

However, the SAXS data of 72 h incubated WT and D187N mutant proteins at pH 2 showed high intensity profiles. Interestingly, the mutant gelsolin showed a dramatic increase in higher order aggregates with an unusual Guinier pattern (inset, Figure 5C). This corroborated a normalized Kratky analysis, where the mutant gelsolin showed the formation of a hyperbola plateau indicating a high level of disorderliness (Figure 5D). Owing to high polydispersity, further analysis and modeling was not possible. This was in contrast to the proteins at pH 7 (72 h incubated) that each showed a distinct peak close to 1.73, depicting their globular nature. Overall, these observations indicated that low pH induces the formation of higher order, aggregation-prone species in the mutant gelsolin which were further characterized using dye-based assays and microscopic analysis.

D187N Mutant Gelsolin Forms Amyloid-like Aggregates at Low pH. We next monitored the aggregation of WT

and D187N gelsolin incubated at different pH buffers using the standard thioflavin T (ThT) fluorescence assay. Enhancement in ThT fluorescence during aggregation is attributed to the formation of fibrillar amyloid-like aggregates.^{26,32} We found an increase in ThT fluorescence for D187N gelsolin protein incubated in pH 2 and 4 buffers only. However, the D187N gelsolin showed significantly high ThT fluorescence on extended incubation at pH 2 (Figure 6A).

When plotted against time, this fluorescence data traced a typical sigmoidal curve with a distinct lag phase of ~47 h followed by an exponential phase of ~150 h that saturated after 200 h. In the case of pH 4 incubated D187N gelsolin, the rise in ThT fluorescence was noted only after more than a month of incubation and was not characterized further. The far-UV CD signal recorded after 150 h of incubation showed a discrete hump at 215 nm, suggesting that mutant gelsolin attained a β -sheet rich conformation (Figure 6B). In contrast, the WT gelsolin exhibited only a loss in CD signal with a nearly unchanged signature.

To further ascertain differences in the aggregate types, a Congo red (CR) binding assay was performed (Figure S8). The mutant protein aggregates showed a distinct red-shift in their CR absorbance spectra that corroborated the formation of amyloid-like aggregates as reported earlier.^{33,34} Further, the TEM images of end-stage aggregates (1 week incubated) showed the presence of a fibrillar population in the case of mutant gelsolin which was characteristically absent in the WT samples (Figure 6C, D). The supporting AFM images showed that while the WT gelsolin formed large spherical, disc-like aggregates of heterogeneous sizes, the mutant gelsolin showed mature fibrils with an average thickness and heights of 4.8 and 8.1 nm, respectively (Figure 6E, F). We next characterized these end-stage fibrillar aggregates by a fibril disaggregation assay followed by peptide mass fingerprinting. The small tryptic fragments generated from disaggregated fibrils showed a top hit-score of 106, matching that of the human gelsolin protein, and a sequence coverage of 42% (Figure 7).

It was found that the identified tryptic peptides matched fragments from the entire protein sequence (Table S3). This also included the previously reported amyloidogenic fragment comprising residues 173–243 present in the G2 domain.³² In all, the data suggested the involvement of intact mutant gelsolin or a major structural component in contrast to the previously described proteolytic pathway mostly driven by 5–8 kDa fragments.^{35,36} At this stage, it was necessary to understand the role of the D187N mutation in the loss of structural integrity of gelsolin and its conversion to an aggregation-prone conformer that forms fibrillar aggregates under low pH conditions.

The D187N Mutation Alters the Structural Integrity of the G2 Domain. To further understand the loss of structural integrity and predisposition to the amyloid state due to a D187N mutation in gelsolin, we carried out constant pH all-atom molecular dynamics simulations. Simulation trajectories at pH 7 and 2 for both the WT and D187N mutant gelsolin were analyzed. Backbone RMSD variations for the D187N mutant at pH 2 during the last ~50 ns showed the highest deviation from the initial starting structure as compared to other systems (Figure S9A). However, only marginal changes in the overall gyration radius (R_g) were observed in all systems (Figure S9B). Additionally, free energy landscapes (FELs) were constructed to sample the lowest free energy conformations attained by the proteins in different systems during the simulations. The Gibbs free energy surfaces were projected using previously analyzed

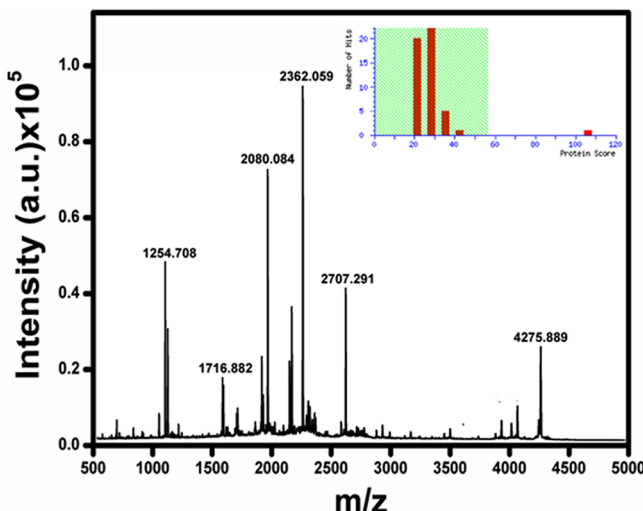


Figure 7. Analysis of end-stage amyloid aggregates using mass spectrometry. Identification of the peptide sequences incorporating amyloid fibrils formed by D187N mutant gelsolin using mass spectrometry. The MALDI-TOF MS spectrum of peptide fragments present in the disaggregated fibrils after treatment with trypsin and subsequent elution in 60% acetonitrile using C18 ZipTip clean up. The inset shows a Mascot score histogram where protein scores greater than 56 are significant ($p < 0.05$). The tryptic fragments generated from disaggregated fibrils showed a top hit-score of 106, matching that of the human gelsolin protein, and a sequence coverage of 42%.

variables: R_g and backbone RMSD. For the WT system at both pHs, the lowest free energy conformations were restricted to the conformational space close to the original starting structure with minimal changes in the gyration radius (Figure S10A, B). However, for D187N gelsolin at both pHs, the conformational subspace drifted, with the lowest free energy conformations having slightly higher R_g values (~2.88 nm) compared to those of the WT system (~2.82 nm) (Figure S10C, D). Interestingly, we found that the D187N mutant gelsolin at pH 2 occupied a larger part of the conformational space. In this system, two separate lowest energy basins could be observed, which might represent metastable states attained by the mutant during simulations (cyan arrows, Figure S10C).

Since gelsolin is a large multidomain protein, mapping the entire pathway of its transition to an amyloid-competent state using constant temperature simulations was computationally challenging. This was due to sampling limitations for major conformational changes in all-atom simulations performed at room temperature (310 K). Thus, we resorted to REMD (replica exchange molecular dynamics) simulations of mutant gelsolin at pH 7 and 2 for sampling conformational changes. To understand its role in the loss of structural integrity in gelsolin, the observations were mainly focused on the G2 domain carrying the D187N mutation. Structural parameters, such as Ca-RMSD, number of protein–solvent contacts, changes in solvent accessibility, and radius of gyration, were studied for D187N mutant gelsolin at pH 7 and 2 using individual replicas in the temperature range of 310–370 K (Figure 8). It is evident that while traversing from low to high temperatures, the protein will partially denature into metastable states. Consequently, the stability of mutant gelsolin under both pH conditions can be sampled in terms of its resistance to lose its structural integrity with temperature increments (at 310, 330, 350, and 370 K). At pH 7 and 2, probability distributions for RMSD of around ~0.5

nm were observed at all temperatures (Figure 8A, B). Interestingly, multiple distributions for protein–solvent contacts were observed at different temperatures in both systems. With the increase in temperatures, the total number of solvent contacts gradually increased for the mutant at pH 2 with the highest number of contacts (~1450) observed at 370 K (Figure 8C, D).

However, at pH 7, even at higher temperatures no such increment in contacts was observed as it remained lower than the system at 310 K. Subsequently, free energy landscapes (FELs) of each system were constructed and projected as a function of RMSD and the number of protein–solvent contacts at different temperatures (Figure S11). For the D187N mutant at pH 2, the lowest free energy conformations showed a marginally higher solvent contact frequency (~50 contacts) as compared to that of corresponding mutant systems at pH 7 at each temperature. Further, we narrowed down our analysis to the G2 domain at 350 K, since the manifestation of D187N mutations could be immediately observed in this domain and can be attributed as a triggering point of aggregation. For sampling, the preferred conformational space of G2 at pH 2 and 7 FELs was plotted as a function of solvent accessible area and number of contacts with the solvent (Figure S12). At pH 2, the G2 domain showed the presence of more than one distributed low free energy basin corresponding to states with higher solvent accessibility and correspondingly more solvent contacts.

On the other hand, the lowest free energy state at pH 7 still showed intact fold architecture with a lower number of solvent contacts. This was also validated through an increased loss in structural architecture within the G2 domain at pH 2 compared to that at pH 7. To further investigate these structural transitions, FELs were constructed using a number of residues forming α -helix and β -sheet formations in the G2 domain. At pH 2, multiple lowest free energy basins were observed, corresponding to structures with reduced helix–beta content and increased unstructured content (black arrows, Figure 8E). However, at pH 7, most of the helical and β -sheet regions were conserved even at 350 K with a single lowest free basin for the system (Figure 8F). The representative structures at pH 2 sampled from the lowest free energy basins show a pertinent loss of structural components with apparent β -coil transitions as was observed as compared to those of the pH 7 system (insets, yellow arrows, Figure 8E, F).

DISCUSSION

Gelsolin amyloidogenesis ensues when a mutation in its G2 domain (core Ca^{2+} binding domain) makes the protein susceptible to furin and MT1-MMP mediated cleavage to produce 5 or 8 kDa amyloidogenic fragments.^{7,36} In fact, the proteolysis pathway, as well as amyloid formation by gelsolin fragments, has been targeted for developing new therapeutic interventions against gelsolin-related amyloidosis.^{18,32,37,38} While aggregation and deposition of these fragments are quite evident, the concomitant physiological environment inside the cell has yet to be investigated. This is important since several secondary pathways contribute to amyloid-associated tissue impairment and death. In the case of gelsolin-related amyloidosis, severe mitochondrial abnormalities along with high serum lactate production have been reported.²¹ Interestingly, modulation of the actin cytoskeleton by the gelsolin also plays a key role in regulating vacuolar H^+ -ATPase (V-ATPase) recycling. Moreover, the modulation of the actin

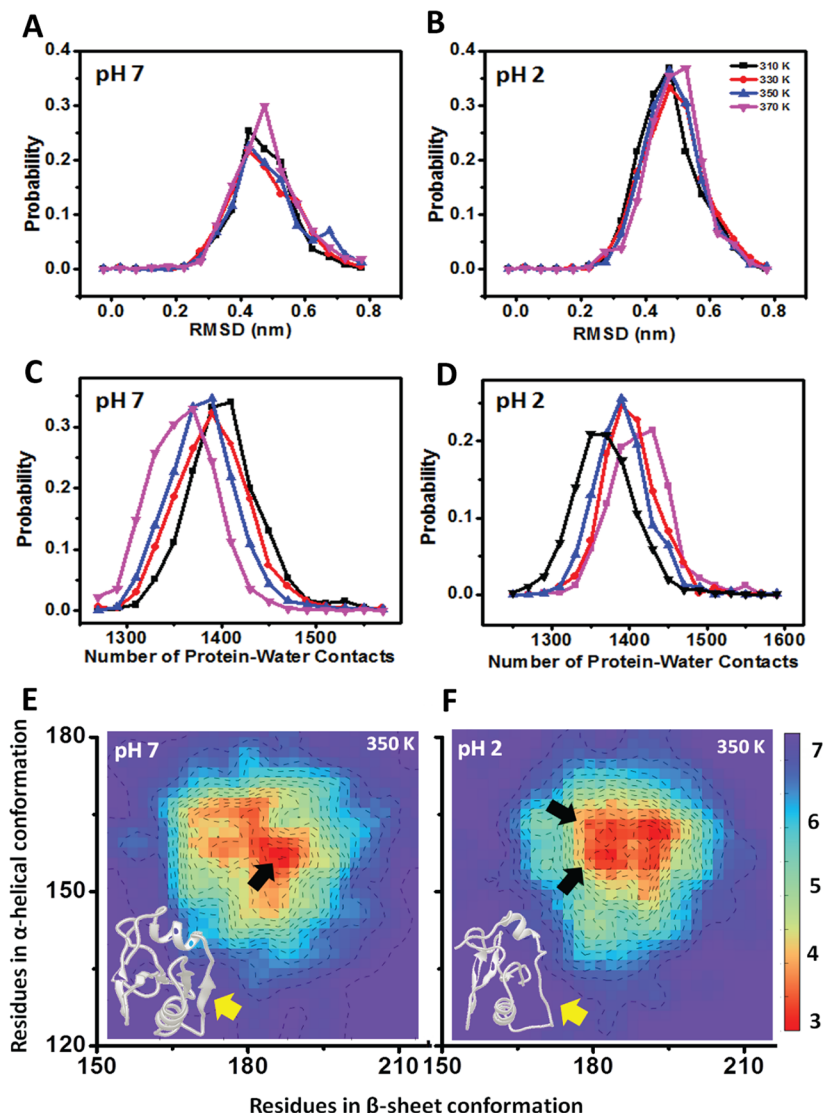


Figure 8. Structural insights of pH-induced perturbations in mutant gelsolin. The probability distribution of backbone RMSD obtained from REMD simulations at pH 7 (A) and pH 2 (B). The probability distribution of the number of protein–water contacts at pH 7 (C) and pH 2 (D). Free energy landscapes (FELs) for the G2 domain of D187N mutant gelsolin. Gibbs free energy surfaces in kcal/mol projected as a function of the number of residues forming an α -helix and β -sheet at pH 7 (E) and pH 2 (F). Black arrows in (E) show the distribution of species with a lower number of secondary structural elements than in (F). Yellow arrows in the insets indicate β -coil transitions in structures extracted from the lowest free energy basins from both FELs.

cortex by Ca^{2+} activated gelsolin represents a common mechanism by which cells regulate their rate of proton secretion.³⁹ Thus, it is very likely that the presence of mutant gelsolin with low Ca^{2+} sensitivity and subdued actin modulation capacity could contribute to the H^+ balance in cellular compartments. During the late/progressive phases of gelsolin amyloidosis, this may further induct an alternate H^+ rich but Ca^{2+} depleted environment, resulting in several alternative aggregation pathways.

To understand the biophysical basis of these alterations, we compared structural stabilities and aggregation propensities of WT and D187N mutant gelsolin proteins under low pH conditions. Although the mutant showed a considerable loss in actin-depolymerization activity, at physiological conditions both mutant and WT gelsolins retained fairly identical global shapes. However, on studying thermal and denaturant mediated unfolding of both proteins, we identified that the D187N mutant showed considerable instability as compared to the WT

(Figure 4). Evidently, the D187N mutation in the G2 domain also incurs a loss in folding cooperativity (lowered C_m value, Table 2), which loosens the structure and increases its hydrodynamic volume, as is apparent in its SEC profile (Figure 2A). The loss in cooperativity and altered domain unwinding in mutant gelsolin was also apparent with an aberrant change in its tertiary structure with an increasing proton (H^+) gradient (Figure 5). These observations support the notion that in multidomain proteins, favorable interactions tether domains together rendering extra stability to individual domains.⁴⁰ Moreover, specific point mutations adversely affect these interactions and thus alter the folding and solvation of individual domains.^{41,42}

In line with the above, mutant gelsolin showed a high aggregation tendency with an increasing proton gradient. The mutant gelsolin formed higher order assemblies (Figure S7) mainly driven by hydrophobic interactions (~4-fold loss in surface hydrophobicity, Figure 5B). This was also confirmed by

SAXS analysis at pH 2 that showed comparatively higher polydispersity in the case of mutant gelsolin (Figure 5C, D). A prolonged incubation for up to 72 h at pH 2 indicated a high degree of disorderness and aggregation in mutant gelsolin as compared to that at the physiological pH (Table 1). In this regard, the aggregation of mutant gelsolin resembles low pH-based partial denaturation of tetrameric transthyretin (TTR) rendering a pro-amyloidogenic state.⁴³ TTR is composed of four noncovalently attached identical polypeptide chains that form an ensemble of structures mostly stabilized by a strong interdomain hydrogen bond network.⁴⁴ In contrast, the hexa-domain architecture of gelsolin is stabilized by the presence of interdomain linkers that covalently tether the domains and enhance their communication.^{12,45} Thus, aggregation at low pH is mostly initiated by oligomerization of the misfolded gelsolin ensemble as evident from the fluorescence, DLS, and SAXS experiments.

On extended incubation at low pH conditions, mutant gelsolin forms ThT responsive aggregates which are fibrillar in nature as observed by TEM and AFM imaging (Figure 6D, F). These amyloid-like fibrils result from a sigmoidal transition constituting oligomerization followed by higher order aggregation of D187N mutant gelsolin similar to other amyloidogenic proteins including the 8 kDa gelsolin fragment.^{26,32,46} Interestingly, fibril disaggregation followed by mass spectrometry suggested the involvement of the entire protein ensemble in amyloid formation (Table S3). Besides, the absence of specific proteolytic factors in our assays indicates that this amyloidogenic pathway is different and possibly an additional furin-independent pathway. A similar alternate pathway involving domain swapping and dimerization of G167R mutant gelsolin has also been reported very recently.⁴⁷ Nevertheless, the possibility of an autocatalytic or acid hydrolytic mechanism releasing amyloidogenic fragments cannot be ruled out. In that case, it may be similar to the role of nicked lysozyme in mediating amyloid formation at acidic pH.⁴⁸ Altogether, low pH oligomerization of the D187N mutant gelsolin acts as a prerequisite and rate-limiting step for amyloid aggregation. Thus, our results suggest the existence of an alternate oligomerization-dependent pathway besides the previously known proteolysis-dependent pathway (Figure 9).

It will be interesting to decipher any structural and kinetic differences in amyloids formed in both pathways through future studies. Insights obtained through MD simulations supported our experimental outcomes where mutant gelsolin at pH 2 showed the highest structural deviation from native architecture substantiated by the presence of alternate low free energy basins in its conformational space. The effect of low pH could be manifested in terms of a higher contact frequency with solvent for mutant gelsolin, signifying possible exposure of hydrophobic core regions. This could be due to loss of compactness in the protein which decreases interdomain communications, resulting in partially opened aggregation-prone states (Figure 8). Apparently, at low pH, the mutation carrying the G2 domain of mutant gelsolin showed loss of both helix and beta contents to form solvent exposed metastable states, separated by small energy barriers. Structural reorganization in the mutant G2 domain was also evident by an overall increase in the number of intramolecular contacts (351) as compared to those of the WT G2 domain (325). Upon analysis of local interactions in the vicinity of mutated residue, the loss of three native hydrogen bonds involving residues N184 and Q164 was apparent (Figure S13). This structural loss has been

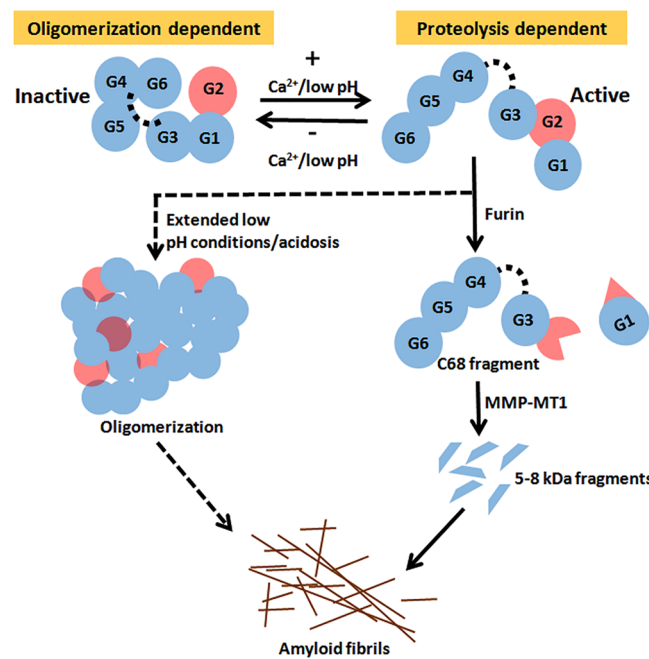


Figure 9. Canonical and proposed aggregation pathways of D187N mutant gelsolin. In the canonical proteolysis-dependent pathway, mutant gelsolin gets cleaved by furin to generate a 68 kDa fragment (C68) that further gets proteolyzed by MT1-MMP-like proteases to produce 5–8 kDa fragments. These 5–8 kDa amyloidogenic peptide fragments later get deposited as amyloid fibrils. During an acidosis scenario, mutant gelsolin may follow an alternate oligomerization-dependent pathway where it skips the proteolytic pathway and forms higher order aggregates that later aggregate into amyloid fibrils.

documented in previous reports that pointed to the loss of β -sheet in G2 as the primary reason for destabilization associated with D187N mutation.⁴⁹ However, more information on the level of structural destabilization in the G2 domain would require ¹⁹F NMR analysis combined with extensive MD simulations.

Perhaps, the observed partially opened conformations could be one of the many triggering states for oligomerization and later aggregation of D187N mutant gelsolin as observed in our biophysical and SAXS experiments. Overall, we show that the pathogenic point mutation in gelsolin protein sufficiently destabilizes its folded architecture under calcium depleted, low pH conditions and can induce amyloid-like assembly. Our study supports the presence of an alternate aggregation mechanism devoid of the canonical proteolytic cleavage in a H⁺ rich but Ca²⁺ depleted environment during progressive stages of gelsolin amyloidosis. This is important since progressive phases of gelsolin amyloidosis accompany a surge in several noncanonical and secondary pathways that contribute to amyloid-associated tissue impairment and death. One of these critical secondary pathways is the rise in the H⁺ gradient inside cellular organelles, including the ER. Our data suggest that the lowering of cellular pH could contribute to the formation of amyloid-like aggregates by D187N mutant gelsolin by a furin/MMP-MT1-independent secondary oligomerization-dependent pathway (Figure 9). In this alternate pathway, partially active mutant gelsolin oligomerizes and may aid in inducing a high amyloid load by acting as amyloidogenic seeds. The existence of similar secondary, proteolysis-independent pathways involving other gelsolin disease mutants, viz. D187Y and N184K, cannot be ruled out and should be investigated in

future studies. The experimental evidence presented here has shed light on the presence of alternate aggregation mechanisms during gelsolin amyloidosis and can help in the design of better therapeutics.

■ ASSOCIATED CONTENT

Supporting Information

The Supporting Information is available free of charge on the ACS Publications website at DOI: [10.1021/acs.biochem.8b00039](https://doi.org/10.1021/acs.biochem.8b00039).

Supporting methods and analysis data, including an actin-depolymerization assay, molecular mass estimation of proteins, secondary structure estimation, tryptophan fluorescence, acrylamide quenching, dynamic light scattering, a Congo Red binding assay, and a list of tryptic peptide fragments; RMSD and radius of gyration variation data; free energy landscape projections of all-atomistic and REMD simulations; hydrogen bond network assessment ([PDF](#))

■ AUTHOR INFORMATION

Corresponding Authors

*E-mail: bkundu@bioschool.iitd.ac.in. Phone: +91-11-26591037.

*E-mail: ashgang@imtech.res.in. Phone: 0172-2636680 ext. 3284.

ORCID®

Bishwajit Kundu: [0000-0002-5786-3144](https://orcid.org/0000-0002-5786-3144)

Present Address

[§]Department of Biochemistry, Deshbandhu College, Delhi University, New Delhi, India.

Author Contributions

B.K. and A. conceived and coordinated the study. A.S. designed, performed, and analyzed the data from the experiments, along with P.A., F.K., and P.R. J.S. performed and analyzed the computational experiments. S.P.S.Y. performed the SAXS experiments and analyzed the data. J.S. and S.P.S.Y. contributed equally to this work. A.S., B.K., and A. wrote the manuscript with contributions from the other authors. All authors approved the final version of the manuscript.

Funding

B.K. and A. are grateful for financial support from the Indian Council of Medical Research[grant number 52/2/2013/BMS] and the Department of Biotechnology, Government of India, New Delhi [grant number BT/PR5474/MED/30/824/2012]. A.S., J.S., and S.P.S.Y. acknowledge scholarship support from ICMR, IIT Delhi, and DST, respectively.

Notes

The authors declare no competing financial interest.

■ ACKNOWLEDGMENTS

The authors acknowledge the synchrotron BM-29 beamline facility at the European synchrotron radiation facility (ESRF), Grenoble, France, for SAXS data collection. The authors thank the Indian Institute of Technology Delhi and the CSIR-Institute of Microbial Technology Chandigarh for infrastructural support. A.S. is indebted to Dr. Dushyant K. Garg and Dr. Saurabh Bansal for technical discussions. The authors acknowledge Arti Kataria, Pankaj Sharma, and Nikita Admane for help in different experiments. The authors also acknowledge

Subodh Jain for technical assistance in performing the mass spectrometry experiments.

■ REFERENCES

- (1) Riek, R., and Eisenberg, D. S. (2016) The activities of amyloids from a structural perspective. *Nature* **539**, 227–235.
- (2) Greenwald, J., and Riek, R. (2010) Biology of amyloid: structure, function, and regulation. *Structure* **18**, 1244–1260.
- (3) Eisenberg, D., and Jucker, M. (2012) The amyloid state of proteins in human diseases. *Cell* **148**, 1188–1203.
- (4) Haass, C., and Selkoe, D. J. (2007) Soluble protein oligomers in neurodegeneration: lessons from the Alzheimer's amyloid beta-peptide. *Nat. Rev. Mol. Cell Biol.* **8**, 101–112.
- (5) Maury, C. P. J., Kere, J., Tolvanen, R., and Delachapelle, A. (1990) Finnish Hereditary Amyloidosis Is Caused by a Single Nucleotide Substitution in the Gelsolin Gene. *FEBS Lett.* **276**, 75–77.
- (6) Kiuru, S. (1998) Gelsolin-related familial amyloidosis, Finnish type (FAF), and its variants found worldwide. *Amyloid* **5**, 55–66.
- (7) Maury, C. P., Liljestrom, M., Boysen, G., Tornroth, T., de la Chapelle, A., and Nurmiaho-Lassila, E. L. (2000) Danish type gelsolin related amyloidosis: 654G-T mutation is associated with a disease pathogenetically and clinically similar to that caused by the 654G-A mutation (familial amyloidosis of the Finnish type). *J. Clin. Pathol.* **53**, 95–99.
- (8) Efebera, Y. A., Sturm, A., Baack, E. C., Hofmeister, C. C., Satoskar, A., Nadasdy, T., Nadasdy, G., Benson, D. M., Gillmore, J. D., Hawkins, P. N., and Rowczencio, D. (2014) Novel gelsolin variant as the cause of nephrotic syndrome and renal amyloidosis in a large kindred. *Amyloid* **21**, 110–112.
- (9) Sethi, S., Theis, J. D., Quint, P., Maierhofer, W., Kurtin, P. J., Dogan, A., and Highsmith, E. W. (2013) Renal Amyloidosis Associated With a Novel Sequence Variant of Gelsolin. *Am. J. Kidney Dis.* **61**, 161–166.
- (10) Solomon, J. P., Page, L. J., Balch, W. E., and Kelly, J. W. (2012) Gelsolin amyloidosis: genetics, biochemistry, pathology and possible strategies for therapeutic intervention. *Crit. Rev. Biochem. Mol. Biol.* **47**, 282–296.
- (11) Peddada, N., Sagar, A., Rathore, Y. S., Choudhary, V., Pattnaik, U. B. K., Khatri, N., Garg, R., and Ashish (2013) Global Shapes of F-actin Depolymerization-competent Minimal Gelsolins INSIGHT INTO THE ROLE OF g2-g3 LINKER IN pH/Ca²⁺ INSENSITIVITY OF THE FIRST HALF. *J. Biol. Chem.* **288**, 28266–28282.
- (12) Garg, R., Peddada, N., Sagar, A., Nihalani, D., and Ashish (2011) Visual Insight into How Low pH Alone Can Induce Actin-severing Ability in Gelsolin under Calcium-free Conditions. *J. Biol. Chem.* **286**, 20387–20397.
- (13) Ashish, Paine, M. S., Perryman, P. B., Yang, L., Yin, H. L., and Krueger, J. K. (2007) Global structure changes associated with Ca²⁺ activation of full-length human plasma gelsolin. *J. Biol. Chem.* **282**, 25884–25892.
- (14) Kislar, J. G., Janmey, P. A., Almo, S. C., and Chance, M. R. (2003) Visualizing the Ca²⁺-dependent activation of gelsolin by using synchrotron footprinting. *Proc. Natl. Acad. Sci. U. S. A.* **100**, 3942–3947.
- (15) Zapun, A., Grammatyka, S., Deral, G., and Vernet, T. (2000) Calcium-dependent conformational stability of modules 1 and 2 of human gelsolin. *Biochem. J.* **350**, 873–881.
- (16) Ratnaswamy, G., Huff, M. E., Su, A. I., Rion, S., and Kelly, J. W. (2001) Destabilization of Ca²⁺-free gelsolin may not be responsible for proteolysis in Familial Amyloidosis of Finnish Type. *Proc. Natl. Acad. Sci. U. S. A.* **98**, 2334–2339.
- (17) Page, L. J., Suk, J. Y., Bazhenova, L., Fleming, S. M., Wood, M., Jiang, Y., Guo, L. T., Mizisin, A. P., Kisilevsky, R., Shelton, G. D., Balch, W. E., and Kelly, J. W. (2009) Secretion of amyloidogenic gelsolin progressively compromises protein homeostasis leading to the intracellular aggregation of proteins. *Proc. Natl. Acad. Sci. U. S. A.* **106**, 11125–11130.
- (18) Van Overbeke, W., Wongsantichon, J., Everaert, I., Verhelle, A., Zwaenepoel, O., Loonchanta, A., Burtnick, L. D., De Ganck, A.,

- Hocheipied, T., Haigh, J., Cuvelier, C., Derave, W., Robinson, R. C., and Gettemans, J. (2015) An ER-directed gelsolin nanobody targets the first step in amyloid formation in a gelsolin amyloidosis mouse model. *Hum. Mol. Genet.* 24, 2492–2507.
- (19) Pirchl, M., Marksteiner, J., and Humpel, C. (2006) Effects of acidosis on brain capillary endothelial cells and cholinergic neurons: relevance to vascular dementia and Alzheimer's disease. *Neurol. Res.* 28, 657–664.
- (20) Pirchl, M., and Humpel, C. (2010) Does acidosis in brain play a role in Alzheimers disease? *Neuropsychiatr. 23*, 187–192.
- (21) Joshi, P. R., Vetterke, M., Hauburger, A., Tacik, P., Stoltzenburg, G., and Hanisch, F. (2014) Functional relevance of mitochondrial abnormalities in sporadic inclusion body myositis. *J. Clin. Neurosci.* 21, 1959–1963.
- (22) Luke, R. G., Allison, M. E. M., Davidson, J. F., and Duguid, W. P. (1969) Hyperkalemia and Renal Tubular Acidosis Due to Renal Amyloidosis. *Ann. Intern. Med.* 70, 1211.
- (23) Bannykh, S. I., Balch, W. E., Kelly, J. W., Page, L. J., and Shelton, G. D. (2013) Formation of Gelsolin Amyloid Fibrils in the Rough Endoplasmic Reticulum of Skeletal Muscle in the Gelsolin Mouse Model of Inclusion Body Myositis: Comparative Analysis to Human Sporadic Inclusion Body Myositis. *Ultrastruct. Pathol.* 37, 304–311.
- (24) Brewer, G. J. (1997) Effects of acidosis on the distribution and processing of the beta-amyloid precursor protein in cultured hippocampal neurons. *Mol. Chem. Neuropathol.* 31, 171–186.
- (25) Santoro, M. M., and Bolen, D. W. (1988) Unfolding free energy changes determined by the linear extrapolation method. 1. Unfolding of phenylmethanesulfonyl alpha-chymotrypsin using different denaturants. *Biochemistry* 27, 8063–8068.
- (26) Srivastava, A., Sharma, S., Sadanandan, S., Gupta, S., Singh, J., Gupta, S., Haridas, V., and Kundu, B. (2017) Modulation of prion polymerization and toxicity by rationally designed peptidomimetics. *Biochem. J.* 474, 123–147.
- (27) Pernot, P., Round, A., Barrett, R., De Maria Antolinos, A., Gobbo, A., Gordon, E., Huet, J., Kieffer, J., Lentini, M., Mattenet, M., Morawe, C., Mueller-Dieckmann, C., Ohlsson, S., Schmid, W., Surr, J., Theveneau, P., Zerrad, L., and McSweeney, S. (2013) Upgraded ESRF BM29 beamline for SAXS on macromolecules in solution. *J. Synchrotron Radiat.* 20, 660–664.
- (28) Zhang, W., Wu, C., and Duan, Y. (2005) Convergence of replica exchange molecular dynamics. *J. Chem. Phys.* 123, 154105–154113.
- (29) Isaacson, R. L., Weeds, A. G., and Fersht, A. R. (1999) Equilibria and kinetics of folding of gelsolin domain 2 and mutants involved in familial amyloidosis-Finnish type. *Proc. Natl. Acad. Sci. U. S. A.* 96, 11247–11252.
- (30) Kazmirski, S. L., Howard, M. J., Isaacson, R. L., and Fersht, A. R. (2000) Elucidating the mechanism of familial amyloidosis-Finnish type: NMR studies of human gelsolin domain 2. *Proc. Natl. Acad. Sci. U. S. A.* 97, 10706–10711.
- (31) Nag, S., Ma, Q., Wang, H., Chumnarnsilpa, S., Lee, W. L., Larsson, M., Kannan, B., Hernandez-Valladares, M., Burtnick, L. D., and Robinson, R. C. (2009) Ca²⁺ binding by domain 2 plays a critical role in the activation and stabilization of gelsolin. *Proc. Natl. Acad. Sci. U. S. A.* 106, 13713–13718.
- (32) Arya, P., Srivastava, A., Vasaikar, S. V., Mukherjee, G., Mishra, P., and Kundu, B. (2014) Selective Interception of Gelsolin Amyloidogenic Stretch Results in Conformationally Distinct Aggregates with Reduced Toxicity. *ACS Chem. Neurosci.* 5, 982–992.
- (33) Giryach, M., Gorbenko, G., Maliyov, I., Trusova, V., Mizuguchi, C., Saito, H., and Kinnunen, P. (2016) Combined thioflavin T-Congo red fluorescence assay for amyloid fibril detection. *Methods Appl. Fluoresc.* 4, 034010.
- (34) Klunk, W. E., Jacob, R. F., and Mason, R. P. (1999) Quantifying amyloid by Congo red spectral shift assay. *Methods Enzymol.* 309, 285–305.
- (35) Ratnaswamy, G., Koepf, E., Bekele, H., Yin, H., and Kelly, J. W. (1999) The amyloidogenicity of gelsolin is controlled by proteolysis and pH. *Chem. Biol.* 6, 293–304.
- (36) Page, L. J., Suk, J. Y., Huff, M. E., Lim, H. J., Venable, J., Yates, J., Kelly, J. W., and Balch, W. E. (2005) Metalloendoprotease cleavage triggers gelsolin amyloidogenesis. *EMBO J.* 24, 4124–4132.
- (37) Verhelle, A., Nair, N., Everaert, I., Van Overbeke, W., Supply, L., Zwaenepoel, O., Peleman, C., Van Dorpe, J., Lahoutte, T., Devogdt, N., Derave, W., Chuah, M. K., VandenDriessche, T., and Gettemans, J. (2017) AAV9 delivered bispecific nanobody attenuates amyloid burden in the gelsolin amyloidosis mouse model (vol. 26, pg 1353, 2017). *Hum. Mol. Genet.* 26, 3030.
- (38) Srivastava, A., Arya, P., Goel, S., Kundu, B., Mishra, P., and Fnu, A. (2015) Gelsolin Amyloidogenesis Is Effectively Modulated by Curcumin and Emetine Conjugated PLGA Nanoparticles. *PLoS One* 10, e0127011.
- (39) Beaulieu, V., Da Silva, N., Pastor-Soler, N., Brown, C. R., Smith, P. J., Brown, D., and Breton, S. (2005) Modulation of the actin cytoskeleton via gelsolin regulates vacuolar H⁺-ATPase recycling. *J. Biol. Chem.* 280, 8452–8463.
- (40) Bhaskara, R. M., and Srinivasan, N. (2011) Stability of domain structures in multi-domain proteins. *Sci. Rep.* 1, 1–9.
- (41) Randles, L. G., Dawes, G. J. S., Wensley, B. G., Steward, A., Nickson, A. A., and Clarke, J. (2013) Understanding pathogenic single-nucleotide polymorphisms in multidomain proteins - studies of isolated domains are not enough. *FEBS J.* 280, 1018–1027.
- (42) Zheng, W. H., Schafer, N. P., and Wolynes, P. G. (2013) Frustration in the energy landscapes of multidomain protein misfolding. *Proc. Natl. Acad. Sci. U. S. A.* 110, 1680–1685.
- (43) Yang, M. F., Lei, M., Bruschweiler, R., and Huo, S. H. (2005) Initial conformational changes of human transthyretin under partially denaturing conditions. *Biophys. J.* 89, 433–443.
- (44) Lai, Z. H., Colon, W., and Kelly, J. W. (1996) The acid-mediated denaturation pathway of transthyretin yields a conformational intermediate that can self-assemble into amyloid. *Biochemistry* 35, 6470–6482.
- (45) Choe, H., Burtnick, L. D., Mejillano, M., Yin, H. L., Robinson, R. C., and Choe, S. (2002) The calcium activation of gelsolin: Insights from the 3 angstrom structure of the G4-G6/actin complex. *J. Mol. Biol.* 324, 691–702.
- (46) Dean, D. N., Das, P. K., Rana, P., Burg, F., Levites, Y., Morgan, S. E., Ghosh, P., and Rangachari, V. (2017) Strain-specific Fibril Propagation by an A beta Dodecamer. *Sci. Rep.* 7, 40787.
- (47) Boni, F., Milani, M., Barbiroli, A., Diomedè, L., Mastrangelo, E., and de Rosa, M. (2018) Gelsolin pathogenic Gly167Arg mutation promotes domain-swap dimerization of the protein. *Hum. Mol. Genet.* 27, 53–65.
- (48) Mishra, R., Sorgjerd, K., Nystrom, S., Nordgarden, A., Yu, Y. C., and Hammarstrom, P. (2007) Lysozyme amyloidogenesis is accelerated by specific nicking and fragmentation but decelerated by intact protein binding and conversion. *J. Mol. Biol.* 366, 1029–1044.
- (49) Kazmirski, S. L., Isaacson, R. L., An, C., Buckle, A., Johnson, C. M., Daggett, V., and Fersht, A. R. (2002) Loss of a metal-binding site in gelsolin leads to familial amyloidosis-Finnish type. *Nat. Struct. Biol.* 9, 112–116.